Regulation of Proton–α Differential Flow by Compressive Fluctuations and Ion-scale Instabilities in the Solar Wind

Xingyu Zhu[1,2] , Daniel Verscharen[2] , Jiansen He[1] , Bennett A. Maruca[3] , and Christopher J. Owen[2]
[1] School of Earth and Space Sciences, Peking University, Beijing 100871, People's Republic of China
[2] Mullard Space Science Laboratory, University College London, Dorking RH5 6NT, UK
[3] Bartol Research Institute and Department of Physics and Astronomy, University of Delaware, Newark, DE 19716, USA

Abstract

Large-scale compressive slow-mode-like fluctuations can cause variations in the density, temperature, and magnetic-field magnitude in the solar wind. In addition, they also lead to fluctuations in the differential flow $U_{p\alpha}$ between α-particles and protons (p), which is a common source of free energy for the driving of ion-scale instabilities. If the amplitude of the compressive fluctuations is sufficiently large, the fluctuating $U_{p\alpha}$ intermittently drives the plasma across the instability threshold, leading to the excitation of ion-scale instabilities and thus the growth of corresponding ion-scale waves. The unstable waves scatter particles and reduce the average value of $U_{p\alpha}$. We propose that this "fluctuating-drift effect" maintains the average value of $U_{p\alpha}$ well below the marginal instability threshold. We model the large-scale compressive fluctuations in the solar wind as long-wavelength slow-mode waves using a multi-fluid model. We numerically quantify the fluctuating-drift effect for the Alfvén/ ion-cyclotron and fast-magnetosonic/whistler instabilities. We show that measurements of the proton–α differential flow and compressive fluctuations from the Wind spacecraft are consistent with our predictions for the fluctuating-drift effect. This effect creates a new channel for a direct cross-scale energy transfer from large-scale compressions to ion-scale fluctuations.

1. Introduction

The solar wind plasma consists of ions and electrons that are continuously energized in the solar corona and expand into the heliosphere. The plasma conditions in this environment are weakly collisional. Therefore, the velocity distribution functions of the ions often develop and maintain nonthermal features. If these features are sufficiently strong, they provide free energy to drive kinetic instabilities (Hellinger et al. 2006; Maruca 2012; Verscharen et al. 2013a; Zhao et al. 2018; Bowen et al. 2020).

Among the ion species in the solar wind, the α-particles are the second-most abundant species after the protons. They typically account for about 1%–5% of the total ion number density and thus about 4%–20% of the total ion mass density (Robbins et al. 1970; Bame et al. 1977). The α-particle abundance shows, on average, a positive correlation with the solar-wind speed (Aellig et al. 2001; Kasper et al. 2007; Alterman & Kasper 2019).

Protons and α-particles often exhibit distinct bulk velocities U_j, where $j = p, \alpha$, respectively. We define the differential flow velocity between α-particles and protons as $\boldsymbol{U}_{p\alpha} = \boldsymbol{U}_\alpha - \boldsymbol{U}_p$. The resulting vector is generally parallel or antiparallel to the local magnetic field (Kasper et al. 2006) and exhibits correlations with U_p, heliocentric distance R, and the collisional age (Neugebauer et al. 1996; Ďurovcová 2019; Stansby et al. 2019; Mostafavi et al. 2022). Kinetic instabilities driven by proton–α differential flow have typical thresholds of order the

local Alfvén speed (Verscharen et al. 2013b)

$$V_A \equiv \frac{B_0}{\sqrt{4\pi n_p m_p}}, \tag{1}$$

where $\boldsymbol{B}_0$ is the background magnetic field, n_p is the proton number density, and m_p is the proton mass. As the solar wind travels away from the Sun, V_A decreases as long as B_0^2 decreases faster with distance than n_p, which is generally true in the inner heliosphere. If we assume that all relevant plasma variables follow monotonic radial profiles and that $\boldsymbol{U}_p$ and $\boldsymbol{U}_\alpha$ follow a ballistic trajectory, this decrease in the Alfvén speed with R leads to an increase in $U_{p\alpha}/V_A$ with R, bringing $U_{p\alpha}$ closer to the local thresholds of the instabilities driven by proton–α differential flow. Once $U_{p\alpha}$ crosses a local instability threshold, small-scale fluctuations in the electromagnetic field grow at the expense of the $U_{p\alpha}$, and, in turn, the instabilities regulate the value of $U_{p\alpha}$ by limiting it to the local threshold (Marsch et al. 1982; Marsch & Livi 1987; Gary et al. 2000a; Verscharen et al. 2013a).

The proton–α differential flow primarily excites two kinds of kinetic instabilities: a group of Alfvén/ion-cyclotron (A/IC) instabilities and the fast-magnetosonic/whistler (FM/W) instability (Gary 1993; Verscharen et al. 2013b; Gary et al. 2016). The parallel FM/W instability has lower thresholds than other α-particle-driven instabilities when β_p is large, while the oblique A/IC instabilities have lower thresholds at large beam density or small β_p (Gary et al. 2000a), where

$$\beta_j \equiv \frac{8\pi n_j k_B T_j}{B_0^2} \tag{2}$$

is the ratio of thermal energy of species j to the magnetic-field energy, n_j is the density of species j, k_B is the Boltzmann

constant, and T_j is the temperature of species j. The FM/W instability threshold strongly depends on $T_{\perp\alpha}/T_{\|\alpha}$, $\beta_{\|p}$ as well as $T_{\|\alpha}/T_{\|p}$ (Gary et al. 2000b), where $T_{\perp j}$ is the temperature of species j perpendicular to the magnetic field, $T_{\|j}$ is the temperature of species j parallel to the magnetic field, and $\beta_{\|j} \equiv \beta_j T_{\|j}/T_j$. Verscharen et al. (2013a) find a new, parallel A/IC instability in the parameter range $1 < \beta_p < 12$. The minimum $U_{p\alpha}$ for driving this parallel A/IC instability ranges from $0.7 V_A$ when $T_{\perp\alpha} = T_{\|\alpha}$ to $0.9 V_A$ when $T_{\|\alpha}/T_{\|p} = 4$, while the threshold for the FM/W instability is about $1.2 V_A$ (Gary et al. 2000a; Li & Habbal 2000). The temperature anisotropy of the α-particles can also significantly reduce the thresholds of parallel A/IC and FM/W instabilities in terms of $U_{p\alpha}$ (Verscharen et al. 2013b).

Only about 2% of the overall solar-wind fluctuations, in terms of their relative fluctuating power, are compressive (Chen 2016). Observations show that slow-mode-like fluctuations are a major component among these compressive fluctuations in the solar wind (Howes et al. 2012; Klein et al. 2012). Slow-mode-like fluctuations are characterized by an anticorrelation between density and magnetic-field strength, a property that these fluctuations share with the magnetohydrodynamics (MHD) slow mode in the low-β_p limit. A large majority of the compressive fluctuations in the solar wind are found to be quasi-stationary pressure-balanced structures, which can be interpreted as highly oblique slow modes, although the exact orientation of their wavevectors and thus their propagation properties are not fully understood (Bavassano et al. 2004; Kellogg & Horbury 2005; Yao et al. 2011, 2013).[4] The three-dimensional eddy shape of the compressive fluctuations is highly elongated along the local mean magnetic field (Chen et al. 2012). The wavevector anisotropy ($k_\perp/k_\|$) of large-scale compressive fluctuations is typically greater than 6 and thus about 4 times greater than the wavevector anisotropy of the Alfvénic fluctuations at the same scale (Chen 2016), where $k_\perp$ and $k_\|$ are the wavenumbers in the directions perpendicular and parallel to the background magnetic field. Therefore, most compressive fluctuations have an angle of propagation greater than $80°$ with respect to the local mean magnetic field. This result is confirmed by the agreement between MHD predictions of slow-mode polarization properties assuming an angle of $88°$ and observations of the compressive fluctuations in the solar wind (Verscharen et al. 2017).

Slow-mode-like fluctuations with large amplitudes cause significant changes in the plasma density, temperature, and magnetic-field strength. This leads to an effect known as the "fluctuating-anisotropy effect" (Verscharen et al. 2016). In this framework, slow-mode-like fluctuations quasiperiodically modify the values of $T_{\perp p}/T_{\|p}$ and $\beta_{\|p}$ at any given point in the plasma, fluctuating around their average values. If these values cross the thresholds for anisotropy-driven kinetic instabilities during this parameter-space trajectory, ion-scale waves grow and scatter the protons, altering the average value of $T_{\perp p}/T_{\|p}$. The combined action of compressive fluctuations and the anisotropy-driven instabilities maintains an average value of $T_{\perp p}/T_{\|p}$ away from the instability thresholds at a

location in parameter space that depends on the amplitude of the large-scale compressive fluctuations.

In this work, we extend the fluctuating-anisotropy effect to a broader "fluctuating-moment framework" by incorporating relative drifts between protons and α-particles. We refer to the modification of $U_{p\alpha}$ in the presence of large-scale compressions and the associated amplitude-dependent reduction of the effective thresholds of drift-driven instabilities as the "fluctuating-drift effect." We hypothesize that long-wavelength slow-mode-like fluctuations are able to lower the effective thresholds of α-particle-driven kinetic instabilities in the solar wind.

In Section 2, we present our understanding of the framework in which slow-mode-like fluctuations modify the effective instability threshold. We present our results showing the dependence of the effective thresholds of A/IC and FM/W instabilities. In Section 3, we test our theoretical results against solar-wind measurements from the Wind spacecraft. We present our results and discuss the limitations and further research directions in Section 4.

2. Analysis of the Fluctuating-drift Effect

2.1. Conceptual Description

Figure 1 illustrates the fundamental concept of the fluctuating-drift effect. In case (a), we assume that no compressive fluctuations are present ($\delta B_\| = 0$) and that $U_{p\alpha 0}$ (i.e., the average $U_{p\alpha}$) is below the threshold value U_{th} for any given α-particle-driven instability. Since $U_{p\alpha} < U_{th}$ at all times, this case corresponds to an overall stable configuration.

In case (b), we now include a slow-mode-like fluctuation with a small amplitude $\delta B_\| \neq 0$. Due to the presence of this fluctuation, all plasma and field parameters participate in the fluctuations according to the polarization properties of the mode. This leads to quasiperiodic fluctuations in $U_{p\alpha}$ around $U_{p\alpha 0}$ and in the instability threshold U_{th} around its average value U_{th0}. These quasiperiodic fluctuations in $U_{p\alpha}$ and U_{th} are in phase (as we see in Section 2.3). In case (b), we assume that the amplitude $\delta B_\|$ is so small that $U_{p\alpha} < U_{th}$ throughout the evolution of the large-scale compression. Therefore, this system remains stable despite the fluctuations in both $U_{p\alpha}$ and U_{th}.

In case (c), we now assume that the amplitude $\delta B_\|$ is so large that $U_{p\alpha} > U_{th}$ for at least a finite time interval during the quasiperiodic evolution of the large-scale compression. We refer to the critical amplitude required to cause $U_{p\alpha} > U_{th}$ at least once as $\delta B_{\|,crit}$. Once $U_{p\alpha} > U_{th}$, A/IC waves or FM/W waves begin to grow due to the excitation of the relevant kinetic instability. We assume the excited instability grows faster than the timescale of the large-scale compression,[5] so that $U_{p\alpha 0}$ is then quickly reduced through wave–particle interactions. We define the amplitude-dependent value of $U_{p\alpha 0}$ for which $U_{p\alpha}$ reaches U_{th} once during the large-scale compression as $U_{p\alpha 0,crit}$. Its value depends on the background plasma conditions and the amplitude of the slow-mode-like compression. In Sections 2.2 through 2.4, we quantify the dependence of $U_{p\alpha 0,crit}$ on $\beta_{\|p}$ and $\delta B_\|/B_0$.

---

[4] We do not invoke non-propagating pressure-balanced structures for our proposed scenario in this article. We only reference to pressure-balanced structures as observational evidence for the slow-mode-like polarization of the compressive fluctuations in the solar wind.

[5] For highly oblique slow-mode waves at scales comparable to the top end of the inertial range of the solar-wind turbulence, this is a good assumption, even if the maximum growth rate of the instabilities is $\sim 10^{-4}\Omega_p$, where Ω_p is the proton cyclotron frequency.
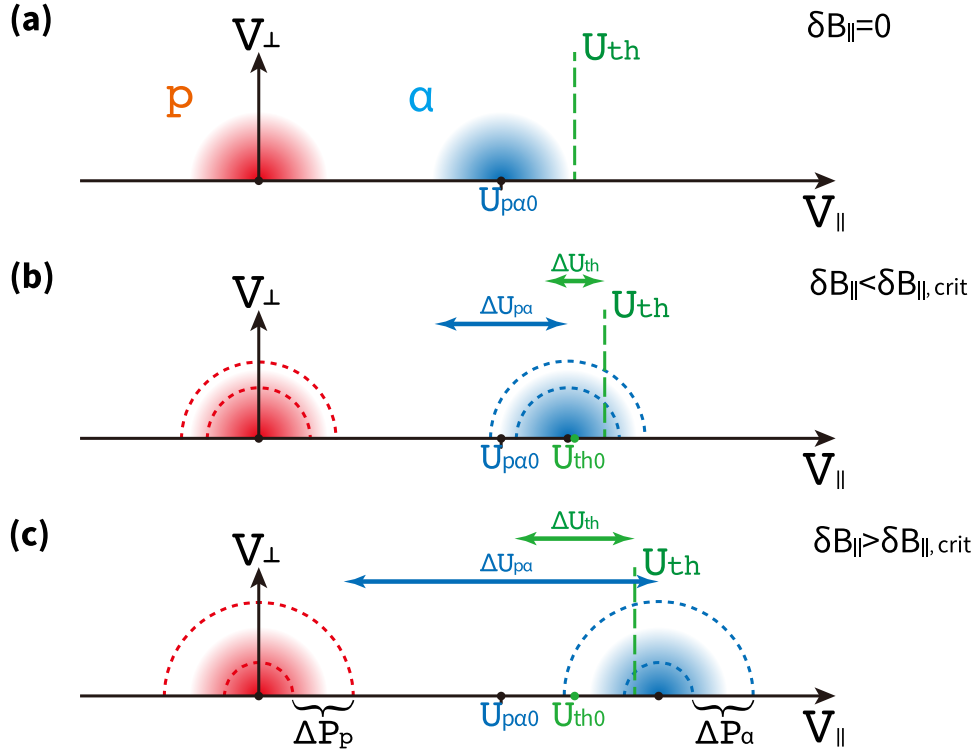
Figure 1. Illustration of the fluctuating-beam effect. We assume the velocity distribution functions of protons (red half-circles) and α-particles (blue half-circles) are initially Maxwellian with the same thermal speed. The initial and instantaneous bulk velocities of each component are represented by black dots. We work in the reference frame of the proton bulk velocity but note that this is not an inertial frame when a slow-mode-like compression is present. (a) Case without slow-mode-like compressions ($\delta B_\parallel = 0$). Both $U_{p\alpha}$ and U_{th} remain constant, i.e., $U_{p\alpha} = U_{p\alpha 0}$ and $U_{th} = U_{th0}$. (b) Case with slow-mode-like compressions with an amplitude $0 < \delta B_\parallel < \delta B_{\parallel,crit}$. This configuration is still stable throughout all phases of the large-scale compression since $U_{p\alpha} < U_{th}$ at all times. (c) Case with slow-mode-like compressions with an amplitude $\delta B_\parallel > \delta B_{\parallel,crit}$. In this case, $U_{p\alpha}$ crosses the instability threshold U_{th} at least one time during the evolution of the large-scale compression. $\Delta U_{p\alpha}$, ΔU_{th}, ΔP_p, and ΔP_α represent the variations of the corresponding quantities, where P_j indicates the scalar pressure of species j.

2.2. Slow-mode-like Fluctuations and Their Effect on α-particle Beams

We solve the linear dispersion relation of slow-mode waves with a multi-fluid plasma model to obtain the associated polarization properties for all relevant quantities. Xie (2014) provides the Plasma Dispersion Relation–Fluid Version (PDRF) code that solves the linearized multi-fluid equations. We obtain all eigenvalues (λ) and eigenvectors (X) of the linearized multi-fluid eigenvalue problem at a fixed wavenumber (k) and with specified background plasma parameters. The number of eigenvalue-eigenvector pairs is $4s + 6$ for each calculation, where s is the total number of plasma species. In our case, $s = 3$.

For the evaluation of the large-scale compression, we consider a homogeneous plasma consisting of electrons, protons, and α-particles with isotropic temperatures ($T_{\parallel j} = T_{\perp j}$) in a uniform background magnetic field $\boldsymbol{B}_0 = B_0 \hat{\boldsymbol{e}}_z$. We only allow for parallel differential background flows. We ignore viscosity and relativistic effects, so the governing fluid equations are

$$\frac{\partial n_j}{\partial t} = -\nabla \cdot (n_j \boldsymbol{U}_j), \qquad (3)$$

$$\frac{\partial \boldsymbol{U}_j}{\partial t} = -\boldsymbol{U}_j \cdot \nabla \boldsymbol{U}_j + \frac{q_j}{m_j}\left(\boldsymbol{E} + \frac{1}{c}\boldsymbol{U}_j \times \boldsymbol{B}\right) - \frac{\nabla P_j}{n_j m_j}, \qquad (4)$$

$$\frac{\partial \boldsymbol{E}}{\partial t} = c\nabla \times \boldsymbol{B} - 4\pi \sum_j q_j n_j \boldsymbol{U}_j, \qquad (5)$$

Table 1
Assumed Plasma Parameters for Our Evaluation of the Linearized Multi-fluid Equations

j	q_j	m_j/m_p	n_{j0}/n_{p0}	$T_{\perp j0}/T_{\parallel j0}$	$T_{\parallel j0}/T_{\parallel p0}$	γ_j
p	$+1$	1	1	1	1	5/3
α	$+2$	4	0.05	1	4	1.61
e	-1	1/1836	1.1	1	1	1.18

$$\frac{\partial \boldsymbol{B}}{\partial t} = -c\nabla \times \boldsymbol{E}, \qquad (6)$$

where q_j is the charge, m_j is the mass, and P_j is the scalar pressure of species j; $\boldsymbol{B}$ is the magnetic field; $\boldsymbol{E}$ is the electric field; and c is the speed of light. We close these equations through the use of the polytropic relation

$$P_j = C_j n_j^{\gamma_j}, \qquad (7)$$

where C_j is a constant and γ_j is the polytropic index. We work in the proton rest frame, which means that $U_p = 0$. Given the background values n_{p0}, $n_{\alpha 0}$, and $U_{p\alpha 0}$, we obtain n_{e0} and U_{e0} from the current-free and charge-neutrality conditions.

We assume highly oblique propagation for our slow mode and set $\theta(\boldsymbol{k}, \boldsymbol{B}_0) = 88°$, where $\theta(\boldsymbol{k}, \boldsymbol{B}_0)$ is the angle between the wavevector $\boldsymbol{k}$ and $\boldsymbol{B}_0$. We focus on the parameter range

$0 < U_{p\alpha0}/V_A < 1.5$ and $0.1 < \beta_{\|p0} < 10$. This range covers the majority of solar-wind conditions at 1 au (Maruca et al. 2011). We list all background parameters of our calculation in Table 1.

In the inner heliosphere, $\gamma_e \sim 1.18$ based on Parker Solar Probe data (Abraham et al. 2022). Observations suggest that $\gamma_p \sim 5/3$ as expected for an adiabatic, mono-atomic gas (Huang et al. 2020; Nicolaou et al. 2020) and $\gamma_\alpha \sim 1.61$ (Ďurovcová 2019). The observed polytropic indexes for α-particles are generally different for the parallel ($\gamma_{\|\alpha}$) and perpendicular ($\gamma_{\perp\alpha}$) pressures and depend on the solar-wind speed (Ďurovcová 2019). In fast wind, $\gamma_{\|\alpha} \sim 1.65$ and $\gamma_{\perp\alpha} \sim 1.57$. In slow wind, $\gamma_{\|\alpha} \sim 1.05$ and $\gamma_{\perp\alpha} \sim 1.24$. Since the largest $U_{p\alpha}$ are observed in fast wind—making fast wind more relevant for our study—we choose the average fast-wind polytropic index $\gamma_\alpha \sim 1.61$ in our analysis below. We discuss the dependence of our results on the particular choice of polytropic indexes in the Appendix. The density ratios and temperature ratios are set according to representative values measured in the solar wind (see Kasper et al. 2008; Maruca et al. 2013).

Our PDRF analysis confirms that, in slow modes, all plasma and field quantities fluctuate, including n_j, T_j, $\boldsymbol{U}_j$, and $\boldsymbol{B}$. This allows us to quantify the variations of $U_{p\alpha}$ and U_{th} to determine $U_{p\alpha,\text{crit}}$.

2.3. Thresholds for A/IC and FM/W Instabilities Depending on Slow-mode Amplitude

Verscharen et al. (2013b) derive two analytical expressions for the parallel A/IC and FM/W instabilities driven by the relative drift between α-particles and protons. According to their derivation, the A/IC instability is excited when

$$U_{p\alpha} > \frac{1}{2}\left[\sigma_1 w_p + V_A + \sqrt{(V_A + \sigma_1 w_p)^2 - 2V_A^2}\right] - \sigma_1 w_p, \quad (8)$$

where $\sigma_1 = 2.4$ and $w_j \equiv \sqrt{2k_B T_j/m_j}$ is the thermal speed of species j. The condition for driving of the FM/W instability is

$$U_{p\alpha} > V_A + \frac{V_A^2}{4\sigma_2 w_\alpha}, \quad (9)$$

where $\sigma_2 = 2.1$. The dimensionless parameters σ_1 and σ_2 are empirical and based on comparisons between the analytical expressions and solutions of the linear Vlasov–Maxwell dispersion relation with $\gamma_m = 10^{-4}\Omega_p$ when $n_\alpha/n_p = 0.05$ and $T_\alpha = 4T_p = 4T_e$, where Ω_p is the proton cyclotron frequency and γ_m is the maximum growth rate of the instabilities. Since we consider isotropic temperatures only, the slow-mode fluctuations impact the instability thresholds by modifying w_p, w_α, $|\boldsymbol{B}|$, and n_p.

Our three-fluid model predicts that the relative amplitudes and the phase differences of w_p and n_p to $\delta B_\|$ do not depend on $k_\| d_p$ when $k_\| d_p \lesssim 10^{-2}$ (not shown here), where $d_p \equiv V_A/\Omega_p$ is the proton inertial length. Hence, we extend the applicability of our results to all slow-mode waves at $k_\| d_p \ll 10^{-2}$. We choose solutions at $k_\| d_p = 3 \times 10^{-4}$ to conduct our further analysis.

Since our assumed background density and temperature ratios are the same as those used by Verscharen et al. (2013b), we directly use Equations (8) and (9) to study the variation of the instability thresholds driven by slow-mode waves. While evaluating these expressions, we ensure that the fluctuating temperatures T_j and densities n_j of all species remain positive during a full slow-mode wave period.
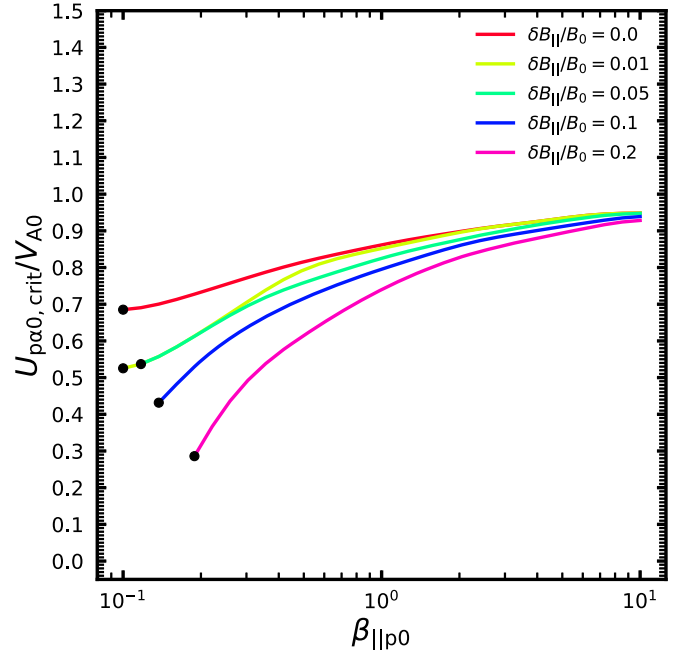
Figure 2. Dependence of the maximum permitted $U_{p\alpha0}$ in terms of $U_{p\alpha0,\text{crit}}/V_{A0}$ on $\beta_{\|p0}$ and $\delta B_\|/B_0$ for the A/IC instability. The normalized amplitude $\delta B_\|/B_0$ varies between 0 and 0.2.

2.4. Determination of the Effective Instability Thresholds

From the dispersion relation, we construct the time series of each quantity $Q(t) = Q_0 + \delta Q(t)$, assuming a plane-wave fluctuation of all quantities with $\delta Q(t) = \text{Re}(\tilde{Q}e^{-i\omega t})$, where $\tilde{Q}$ represents the complex amplitude of quantity Q, ω is the wave frequency, and $\text{Re}(\cdot)$ extracts the real part of a complex variable. We calculate the time series of $U_{p\alpha}(t)$ and $U_{th}(t)$. In general, $\delta Q(t)$ is in phase or antiphase with $\delta B_\|(t)$. By analyzing $U_{p\alpha}(t)$ and $U_{th}(t)$ as functions of t and $\delta B_\|/B_0$, we determine $\delta B_{\|,\text{crit}}/B_0$ depending on $U_{p\alpha0}/V_{A0}$ and $\beta_{\|p0}$, where V_{A0} and $\beta_{\|p0}$ represent the values of V_A and $\beta_{\|p}$ in the limit $\delta B_\| \to 0$.

2.4.1. Fluctuating-drift Effect for the A/IC Instability

Figure 2 shows the dependence of $U_{p\alpha0,\text{crit}}$ on $\beta_{\|p0}$ and $\delta B_\|/B_0$ for the A/IC instability. When there is no slow-mode wave ($\delta B_\|/B_0 = 0$), the A/IC instability threshold changes slowly from $\sim 0.7V_{A0}$ at $\beta_{\|p0} = 0.1$ to $\sim 0.95V_{A0}$ at $\beta_{\|p0} = 10$. This case corresponds to the classical limit in a homogeneous plasma without large-scale compressions.

When a small-amplitude slow-mode wave ($\delta B_\|/B_0 = 0.01$) is present, $U_{p\alpha0,\text{crit}}$ decreases compared to the classical case. The decrease of $U_{p\alpha0,\text{crit}}$ is more significant at $\beta_{\|p0} \lesssim 1$. However, $U_{p\alpha0,\text{crit}}$ is still greater than $0.85V_{A0}$ at $\beta_{\|p0} > 5$ even at large wave amplitudes ($\delta B_\|/B_0 \sim 0.2$). Our solutions break down at low $\beta_{\|p0}$ first, as the wave amplitude increases. These are parameter regimes, in which our linear framework produces negative densities or temperatures, which is unphysical. We mark these breakdown points as black dots at the low-$\beta_{\|p0}$ end of our solution plots.

2.4.2. Fluctuating-drift Effect for the FM/W Instability

Figure 3 has the same format as Figure 2 but shows the FM/W instability thresholds. Unlike the case of the A/IC instability, the effective FM/W instability threshold decreases
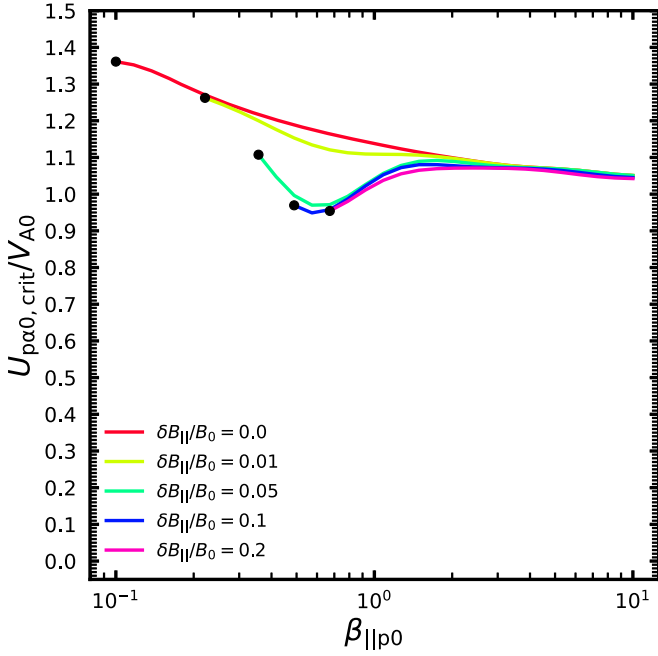
Figure 3. Dependence of the maximum permitted $U_{p\alpha0}$ in terms of $U_{p\alpha0,\mathrm{crit}}/V_{A0}$ on $\beta_{\|p0}$ and $\delta B_\|/B_0$ for the FM/W instability. The normalized amplitude $\delta B_\|/B_0$ varies between 0 and 0.2.

from $\sim 1.35 V_{A0}$ at $\beta_{\|p0} \sim 0.1$ to $\sim 1.05 V_{A0}$ at $\beta_{\|p0} \sim 10$ when $\delta B_\|/B_0 = 0$. The slow-mode fluctuations mainly affect the FM/W instability thresholds at $\beta_{\|p0} < 2$. $U_{p\alpha0,\mathrm{crit}}$ is reduced as the wave amplitude increases. At $\beta_{\|p0} > 2$, the curves in our figure approximately overlap as long as our method provides physical solutions.

3. Comparison with Observations

We compare our theoretical predictions from Section 2 with measurements of protons, α-particles, and compressive fluctuations in the solar wind recorded by the Wind spacecraft at 1 au. We use data from the two Faraday cups that belong to the Solar Wind Experiment (Ogilvie et al. 1995). They generate an ion spectrum with ~ 90 s cadence in most situations. We base our analysis on the nonlinear fitting routine provided by Maruca (2012). This procedure provides us with the plasma density, velocity, and temperature for both protons and α-particles. It incorporates magnetic-field measurements with a cadence of 3 s from the Magnetic Field Investigation (Lepping et al. 1995) instrument to determine the parallel and perpendicular components of temperature and velocity. The procedure also provides the differential flow $U_{p\alpha}$ between α-particles and protons, assuming it aligns with the magnetic-field direction. This data set spans from 1994 November 21 to 2010 July 26 and contains 2,148,228 ion spectra, after removing measurements near the Earth's bow shock or with poor data quality. We divide the data set into nonoverlapping 1 hr intervals. We exclude all intervals with data gaps greater than 20 minutes from further analysis.

For each 1 hr interval, we calculate the average values n_{p0}, T_{p0}, $U_{p\alpha0}$, V_{A0}, and B_0. We then obtain the average $\beta_{\|p0}$ and the average $U_{p\alpha0}/V_{A0}$ from these averages. For the amplitude of the compressive fluctuations, we use the rms value of $\delta|\boldsymbol{B}|$, denoted as $\delta|\boldsymbol{B}|_{\mathrm{rms}}$, instead of $\delta B_\|$, to avoid the impact of inaccuracies in the determination of the parallel magnetic-field direction. We bin the data into eight $\beta_{\|p0}$ ranges from 0.1 to 10

on a logarithmic scale. For each $\beta_{\|p0}$ bin, we divide the sub-data set into 30 bins of $\delta|\boldsymbol{B}|_{\mathrm{rms}}/B_0$ in the range from 0 to 1. We then calculate the probability density function (PDF) of $U_{p\alpha0}/V_{A0}$ for each $\delta|\boldsymbol{B}|_{\mathrm{rms}}/B_0$ bin.

Figure 4 shows the PDF of solar-wind data in the $U_{p\alpha0}/V_{A0}$-$\delta|\boldsymbol{B}|_{\mathrm{rms}}/B_0$ plane for six different $\beta_{\|p0}$ ranges. We also overplot the effective instability threshold $U_{p\alpha0,\mathrm{crit}}/V_{A0}$ (black curve) for the A/IC instability. The parameter space below the effective instability threshold represents the stable region. The PDF of the measured data is largely confined to this stable parameter space in all cases shown. Only an insignificant number of points are beyond the thresholds. We find that $U_{p\alpha0,\mathrm{crit}}/V_{A0}$ decreases with $\delta|\boldsymbol{B}|_{\mathrm{rms}}/B_0$, and the PDFs of our measured data broadly follow this trend. $U_{p\alpha0,\mathrm{crit}}$ bounds the data well in the stable region, especially for $\beta_{\|p0} < 0.5$. At $\beta_{\|p0} \sim 0.75$, the decrease of the maximum $U_{p\alpha0}/V_{A0}$ is steeper than the decrease in $U_{p\alpha0,\mathrm{crit}}$, while in the high-$\beta_{\|p0}$ range, the data points locate farther away from the $U_{p\alpha0,\mathrm{crit}}$ curve. This finding is consistent with our concept that large-scale slow-mode-like fluctuations regulate $U_{p\alpha0}$ through the fluctuating-drift effect. Some data points lie in the parameter space in which our linear model breaks down when $\beta_{\|p0} \sim 0.13$, which is indicated by the vertical line. We emphasize that our results are strictly only valid for $\delta|\boldsymbol{B}|_{\mathrm{rms}}/B_0 \ll 1$, when the linear assumption is valid. We mark a relative amplitude of $\delta|\boldsymbol{B}|_{\mathrm{rms}}/B_0 = 0.2$ with a black arrow in each panel in Figures 4 and 7 (see Appendix) to indicate a reasonable limit for the application of our model.

4. Discussion and Conclusions

We introduce the new concept of the "fluctuating-drift effect" as part of a broader "fluctuating-moment framework." The fluctuating-drift effect describes a link between large-scale compressive fluctuations and small-scale kinetic instabilities driven by relative drifts between ion components in collisionless plasmas. In the solar wind, long-period slow-mode-like fluctuations modulate the background plasma parameters, including n_j, T_j, B, $U_{p\alpha}$, and U_{th}. Once $U_{p\alpha0}$ is greater than the amplitude-dependent critical value $U_{p\alpha0,\mathrm{crit}}$, this slow-mode modulation creates unstable conditions for the growth of beam-driven kinetic micro-instabilities. These micro-instabilities generate waves on a timescale much shorter than the period of the slow-mode-like fluctuations. The separation of time-scales is very large in the solar wind as we show in the following. We estimate the typical slow-mode wave frequency of waves with a wavelength comparable to the top end of the inertial range of solar-wind turbulence at heliocentric distances of about 1 au as (Tu & Marsch 1995; Bruno & Carbone 2013)

$$\omega_s \sim k_\| d_p \sqrt{\beta_p} \Omega_p \sim 10^{-6} \Omega_p, \quad (10)$$
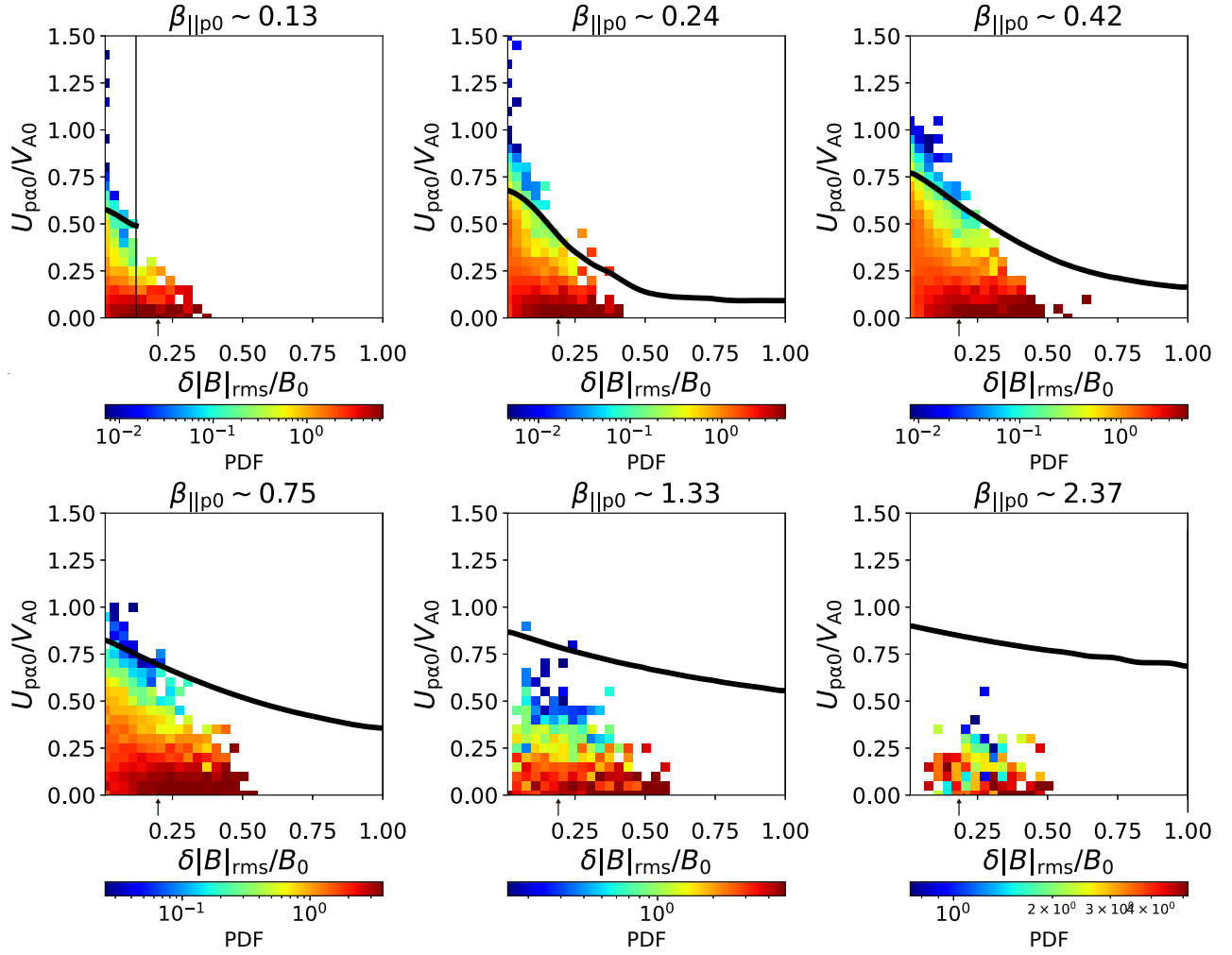
where $k_\| d_p \sim 10^{-6}$ and $0.1 < \beta_p < 10$ under typical plasma conditions for our study. The typical relevant maximum growth rate of the beam-driven instabilities is

$$\gamma_m \sim 10^{-4} - 10^{-3} \Omega_p \quad (11)$$

according to observations (Klein et al. 2018) and simulations (Klein et al. 2017). Therefore, we find

$$\gamma_m \gg \omega_s. \quad (12)$$

Equation (12) is a critical condition for the applicability of our model.

Figure 4. Comparison of our theoretical predictions for the effective instability thresholds $U_{p\alpha0,crit}$ with observations from Wind. We show the comparison for six different $\beta_{\|p0}$ values. The color-coding represents the binned PDFs of 1 hr averaged $U_{p\alpha0}/V_{A0}$ for each $\delta|\boldsymbol{B}|_{rms}/B_0$ bin. The thick solid black curves show the theoretical effective thresholds $U_{p\alpha0,crit}$ for the A/IC instability from Section 2. The vertical black line marks the amplitude above which our linear model breaks down, which is only the case in the first panel. The arrows in each panel below the abscissa indicate the amplitude $\delta|\boldsymbol{B}|_{rms}/B_0 = 0.2$, the approximate limit of validity of the linear model.

The scattering of α-particles by the unstable waves is the main contributor to the reduction of the local $U_{p\alpha}$ and hence to the reduction of the average $U_{p\alpha0}$. This process maintains $U_{p\alpha0}$ well below the classical (average) instability thresholds U_{th0} in a homogeneous plasma. The difference between U_{th0} and $U_{p\alpha0,crit}$ depends on the amplitude of the compressive fluctuations. The effective threshold $U_{p\alpha0,crit}$ decreases with increasing $\delta B_{\|}/B_0$. If $U_{p\alpha0} > U_{p\alpha0,crit}$, the plasma becomes unstable at least for a portion of each compressive fluctuation period. Otherwise, if $U_{p\alpha0} < U_{p\alpha0,crit}$, the plasma is stable throughout the evolution of the slow-mode compression even though the instantaneous $U_{p\alpha}$ varies.

We quantify the dependence of $U_{p\alpha0,crit}$ on the background plasma parameters and the compression amplitude for A/IC and FM/W instabilities. For the A/IC instability, $U_{p\alpha0,crit}$ decreases with increasing slow-mode wave amplitude. For the FM/W instability, $U_{p\alpha0,crit}$ is significantly reduced at finite slow-mode wave amplitudes when $\beta_{\|p0} \lesssim 1$ compared to U_{th0}. We note, however, that the validity of our linear model for the slow-mode-like fluctuations is questionable even at smaller amplitudes.

Although solar-wind turbulence is a nonlinear process, its fluctuations display many properties that are similar to the properties of linear waves (He et al. 2011; Howes et al. 2012; Chen et al. 2013). A large body of observational work (Yao et al. 2011; Chen et al. 2012; Howes et al. 2012; Klein et al. 2012; Verscharen et al. 2017; Šafránková et al. 2021) suggests the presence of slow-mode-like fluctuations in the solar wind although the origin of these fluctuations is still unclear. According to linear theory, classical slow-mode waves are strongly damped in a homogeneous Maxwellian plasma, especially at intermediate to high β_p and when $T_e \lesssim T_p$ (Barnes 1966). Their confirmed existence in the solar wind is thus a major outstanding puzzle in space physics. Possible explanations for this discrepancy between theory and observations include the passive advection of slow-mode-like fluctuations through the dominant Alfvénic turbulence (Schekochihin et al. 2009, 2016), the fluidization of compressive plasma fluctuations by anti-phase-mixing (Parker et al. 2016; Meyrand et al. 2019), or the suppression of linear damping through effective plasma collisionality by particle scattering on micro-instabilities (Riquelme et al. 2015; Verscharen et al. 2016).

Our comparisons of the effective instability thresholds of the A/IC instability with measurements from the Wind spacecraft show that the effective instability thresholds bound the distribution of observed $U_{p\alpha 0}$ values well. This result is consistent with our predictions for the fluctuating-drift effect. We use this observation to justify our use of linear multi-fluid theory to the large-scale compressions in the solar wind.

Our results are largely independent of the averaging time for the definition of the background drift speed $U_{p\alpha 0}$. To illustrate this point, we make the following comparison. In our data set, the average d_p is about 98 km, and the average solar-wind speed is about $426\,\mathrm{km\,s^{-1}}$. Therefore, the convection time of slow-mode waves with $k_\parallel d_p \sim 3 \times 10^{-4}$ is about 80 minutes. Under typical solar-wind conditions ($0.1 < \beta_{\parallel p0} < 10$ and $0 < U_{p\alpha 0}/V_{A0} < 1.5$), the phase speed for these slow-mode waves ranges from $\sim 0.4 V_{A0}$ to $\sim V_{A0}$ based on multi-fluid calculations. Hence, the periods of these waves are between ~ 11.6 and $\sim 29\,\mathrm{hr}$. The characteristic growth time for the instability is about 16 minutes. Therefore, during the 1 hr averaging interval, the spacecraft approximately measures $1/20$ wave periods on average. During this phase, the instability has sufficient time to reduce the local drift velocity of the α-particles, as required by our set of assumptions.

Our model for the slow-mode-like compressions is based on the linearized multi-fluid equations. This linearization is only valid when $\delta B_\parallel / B_0 \ll 1$. Nevertheless, linear predictions often describe the solar wind well, even when the fluctuation amplitude is greater than justifiable based on the linear assumption (Chen et al. 2012; Howes et al. 2012; Verscharen et al. 2017). To some degree, the good agreement between our model predictions and our observations in Figure 4 supports our application of linear theory beyond the very-small-amplitude limit a posteriori. We emphasize at this point, however, that our framework based on linear predictions is strictly applicable only when $\delta B_\parallel / B_0 \ll 1$.

The slow-mode-like compressions provide a self-consistent parallel electric field $E_\parallel \sim \nabla P_e$. In our instability analysis, we implicitly treat this large-scale electric field as constant due to the large spatial and temporal scale separation between the slow-mode wave and the instability. Such a constant $E_\parallel$ impacts the (assumed to be constant) bulk speed of the local background plasma for the instabilities. In our instability analysis, the local background bulk velocity of the plasma is defined as the superposition of the global background plasma velocity vector and the local bulk velocity fluctuation vector of the slow-mode wave. We evaluate the instability criteria in the reference frame in which the local proton bulk velocity is zero. This choice of reference frame does not affect the physics of the kinetic instability.

The instability thresholds and thus the fluctuating-drift effect depend on more parameters than we can explore in this work. For example, the thresholds for the A/IC and FM/W instabilities depend on $T_{\perp \alpha}/T_{\parallel \alpha}$, $\beta_{\parallel p}$, and $\beta_{\parallel \alpha}$ (Verscharen et al. 2013b). The thresholds for both instabilities have a modest dependence on n_α/n_p in the range of 0.01–0.05, which is typical in both the slow wind and fast wind (Bame et al. 1977; Kasper et al. 2007). Two-dimensional simulations of the FM/W instability under solar-wind conditions show that, when $U_{p\alpha 0}/V_{A0} \approx 1.5$, γ_m does not change with $T_{\parallel e}/T_{\parallel p}$ and only slightly decreases as $T_{\perp p}/T_{\parallel p}$ and $T_{\perp \alpha}/T_{\parallel \alpha}$ increase from 0.5 to 1 (Gary et al. 2000a). The dependence of our results on these other plasma parameters merits future investigation.

Relative drifts and temperature anisotropies often occur together. For example, hybrid simulations of α-particle-driven drift instabilities (Ofman & Viñas 2007; Ofman et al. 2022) show that a Maxwellian α-particle population with sufficiently large drift speed drives A/IC instabilities, which then create temperature anisotropy in the α-particle population through velocity-space diffusion. During the nonlinear evolution of this combined kinetic process, the α-particles develop a marginally stable temperature anisotropy, and the drift speed decreases. Plasma turbulence is also capable of generating temperature anisotropy in the α-particle component. However, simulations suggest that the instability-induced generation of temperature anisotropy is more efficient than the turbulence-induced generation of temperature anisotropy in the α-particle component (Ofman & Viñas 2007). This complex interplay between various kinetic processes highlights that a general fluctuating-moment framework is necessary that includes the impact of large-scale fluctuations on all kinetic micro-instabilities.

The fluctuating-drift effect is a consequence of the turbulent nature of the solar wind. This inhomogeneity leads to lower effective instability thresholds compared to homogeneous plasmas. We anticipate that a similar fluctuating-drift effect also applies to proton-beam-driven instabilities. Our work suggests that, through the lower effective instability thresholds, kinetic micro-instabilities are likely to remove more free energy from the α-particle drift globally than previously expected so that instabilities are probably even more important than previously assumed (Verscharen et al. 2015).

Appendix
Dependence on Polytropic Indexes

Plasma descriptions typically fall in one of two categories: fluid or kinetic descriptions. These two approaches do not necessarily lead to the same results even at large fluid scales due to the assumed pressure closure of the fluid equations. The compressive behavior of slow-mode-like fluctuations at large scales depends on the choice of the effective polytropic indexes γ_j of the involved plasma species. For large-scale kinetic slow modes, the effective polytropic indexes are $\gamma_e = 1$ and $\gamma_p = 3$ (Gary 1993). This choice represents one-dimensionally adiabatic protons and isothermal electrons. It is consistent with the kinetic slow-mode dispersion relation $\omega_s \approx k_\parallel c_s$ (Gary 1993; Narita & Marsch 2015; Verscharen et al. 2017), where

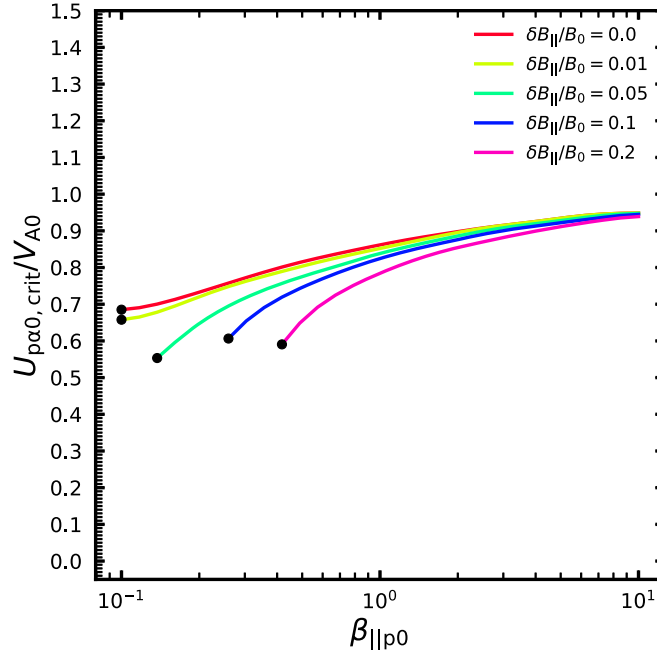$$c_s = \sqrt{\frac{3 k_B T_p + k_B T_e}{m_p}} \qquad (A1)$$

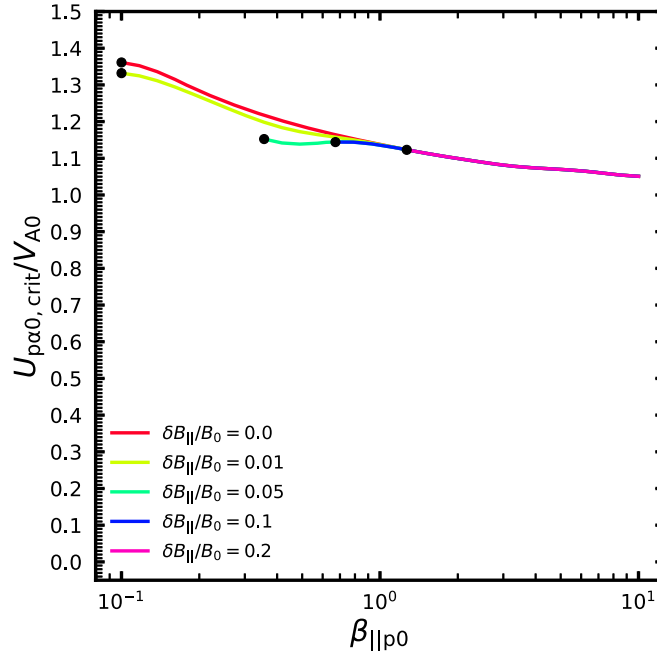**Figure 5.** Same as Figure 2 but using $\gamma_e = 1$, $\gamma_p = 3$, and $\gamma_\alpha = 3$.

Figure 6. Same as Figure 3 but using $\gamma_e = 1$, $\gamma_p = 3$, and $\gamma_\alpha = 3$.

is the phase speed of slow-mode waves in an electron–proton plasma.

We repeat our analysis with these values for a comparison with the results using polytropic indexes consistent with observations of the effective polytropic indexes (Figures 2 through 4). We show the dependence of $U_{p\alpha0,\text{crit}}/V_{A0}$ on $\beta_{\|p0}$ and $\delta B_{\|}/B_0$ for the A/IC and FM/W instabilities in Figures 5 and 6, where we use $\gamma_e = 1$, $\gamma_p = 3$, and $\gamma_\alpha = 3$.

A comparison between Figures 2 and 5 shows insignificant differences in terms of the modified drift thresholds. Only the breakdown points extend to lower $\beta_{\|p0}$ when using the observed

polytropic indexes. The differences between Figures 3 and 6 are significant in the range of typical $\beta_{\|p0}$ values for the solar wind. For $0.5 < \beta_{\|p0} < 1$, the instability takes place for sub-Alfvénic $U_{p\alpha0}$ when $\delta B_{\|}/B_0 \geqslant 0.5$, while, under the assumptions applied in Figure 6, the effective thresholds are always super-Alfvénic in this parameter range.

For completeness, we compare our predictions for $\gamma_e = 1$, $\gamma_p = 3$, and $\gamma_\alpha = 3$ with measurements by the Wind spacecraft in Figure 7. Since the dependence of our results on the particular choice of polytropic indexes is small in the explored parameter space, also this comparison confirms that our
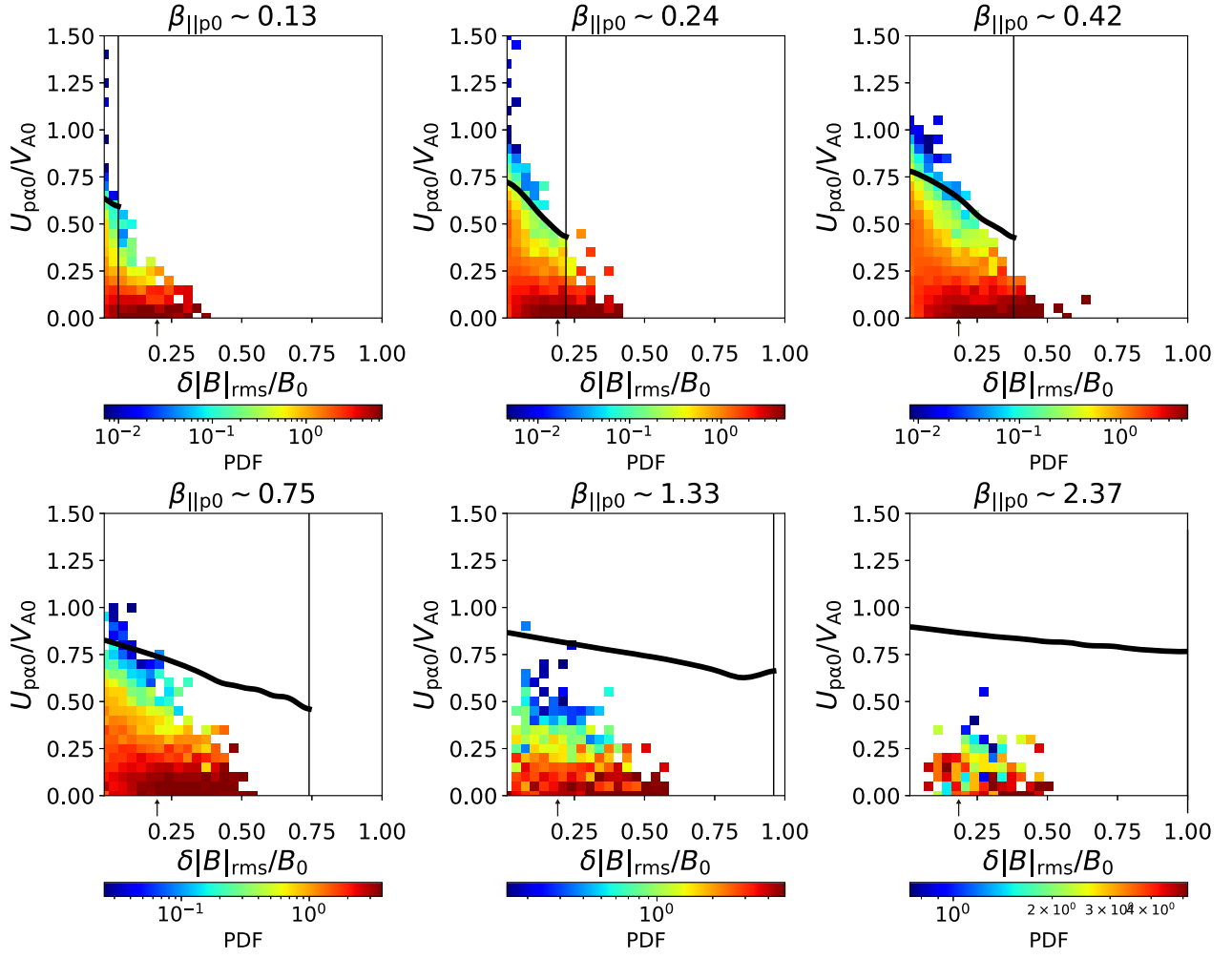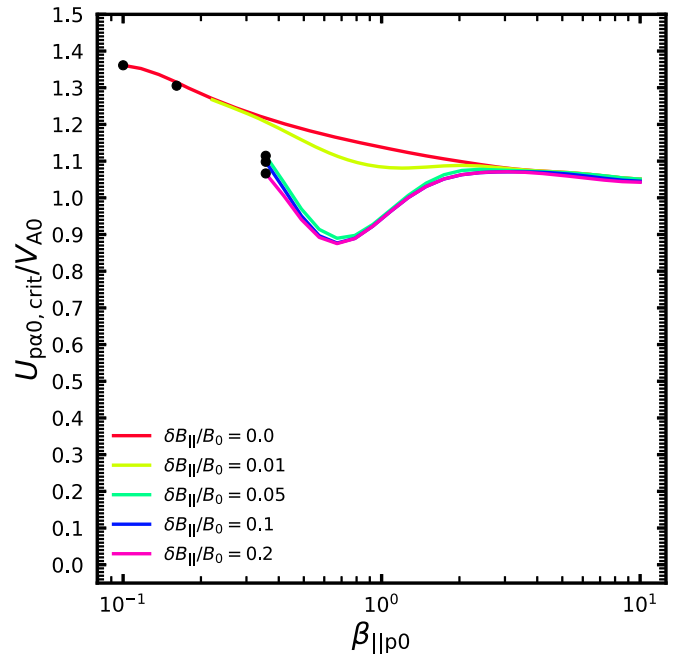
Figure 7. Same as Figure 4 but using $\gamma_e = 1$, $\gamma_p = 3$, and $\gamma_\alpha = 3$. The vertical black lines mark in each panel the amplitude above which our linear model breaks down. The arrows in each panel below the abscissa indicate the amplitude $\delta|\boldsymbol{B}|_{rms}/B_0 = 0.2$, the approximate limit of validity of the linear model.
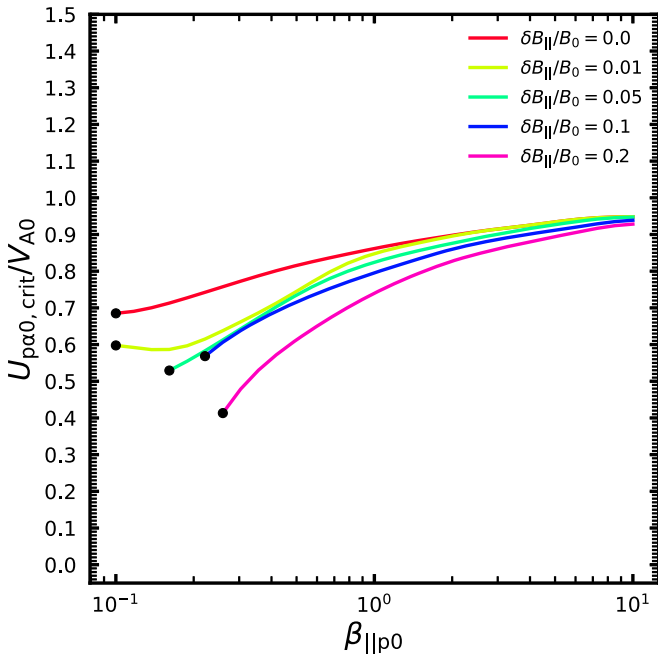
Figure 8. Same as Figure 2 but using $\gamma_e = 1.18$, $\gamma_p = 5/3$, and $\gamma_\alpha = 1.15$.

Figure 9. Same as Figure 3 but using $\gamma_e = 1.18$, $\gamma_p = 5/3$, and $\gamma_\alpha = 1.15$.

theoretical curves limit the data distribution well within the stable parameter space.

Since the polytropic index of the α-particles differs significantly between slow wind and fast wind (Ďurovcová 2019), Figures 8 and 9 show our analysis with the average slow-wind polytropic index $\gamma_\alpha = 1.15$ for a comparison with the fast-wind case of $\gamma_\alpha = 1.61$ (Figures 2 and 3). There is a noticeable difference between Figures 2 and 8, in that the smallest effective threshold for $\delta B_\parallel / B_0 = 0.01$ appears at $\beta_{\parallel p0} \sim 0.16$ in the slow-wind case. The differences between Figures 3 and 9 are also significant. The effective thresholds decrease to lower values for $\delta B_\parallel / B_0 \geqslant 0.05$ in the slow-wind case compared to the fast-wind case.

ORCID iDs

Xingyu Zhu ⬤ https://orcid.org/0000-0002-1541-6397
Daniel Verscharen ⬤ https://orcid.org/0000-0002-0497-1096
Jiansen He ⬤ https://orcid.org/0000-0001-8179-417X
Bennett A. Maruca ⬤ https://orcid.org/0000-0002-2229-5618
Christopher J. Owen ⬤ https://orcid.org/0000-0002-5982-4667

References

Abraham, J. B., Verscharen, D., Wicks, R. T., et al. 2022, ApJ, 941, 145
Aellig, M. R., Lazarus, A. J., & Steinberg, J. T. 2001, GeoRL, 28, 2767
Alterman, B. L., & Kasper, J. C. 2019, ApJL, 879, L6
Bame, S. J., Asbridge, J. R., Feldman, W. C., & Gosling, J. T. 1977, JGR, 82, 1487
Barnes, A. 1966, PhFl, 9, 1483
Bavassano, B., Pietropaolo, E., & Bruno, R. 2004, AnGeo, 22, 689
Bowen, T. A., Mallet, A., Huang, J., et al. 2020, ApJS, 246, 66
Bruno, R., & Carbone, V. 2013, LRSP, 10, 2
Chen, C. H. K. 2016, JPlPh, 82, 535820602
Chen, C. H. K., Boldyrev, S., Xia, Q., & Perez, J. C. 2013, PhRvL, 110, 225002
Chen, C. H. K., Mallet, A., Schekochihin, A. A., et al. 2012, ApJ, 758, 120
Ďurovcová, T., Šafránková, J., & Němeček, Z. 2019, SoPh, 294, 97
Gary, S. P. 1993, Theory of Space Plasma Microinstabilities (New York: Cambridge University Press)
Gary, S. P., Jian, L. K., Broiles, T. W., et al. 2016, JGRA, 121, 30
Gary, S. P., Yin, L., Winske, D., & Reisenfeld, D. B. 2000a, GeoRL, 27, 1355
Gary, S. P., Yin, L., Winske, D., & Reisenfeld, D. B. 2000b, JGR, 105, 20,989
He, J., Marsch, E., Tu, C., Yao, S., & Tian, H. 2011, ApJ, 731, 85
Hellinger, P., Trávníček, P., Kasper, J. C., & Lazarus, A. J. 2006, GeoRL, 33, L09101
Howes, G. G., Bale, S. D., Klein, K. G., et al. 2012, ApJL, 753, L19
Huang, J., Kasper, J. C., Vech, D., et al. 2020, ApJS, 246, 70
Kasper, J. C., Lazarus, A. J., & Gary, S. P. 2008, PhRvL, 101, 261103
Kasper, J. C., Lazarus, A. J., Steinberg, J. T., Ogilvie, K. W., & Szabo, A. 2006, JGRA, 111, A03105
Kasper, J. C., Stevens, M. L., Lazarus, A. J., Steinberg, J. T., & Ogilvie, K. W. 2007, ApJ, 660, 901
Kellogg, P. J., & Horbury, T. S. 2005, AnGeo, 23, 3765
Klein, K. G., Alterman, B. L., Stevens, M. L., Vech, D., & Kasper, J. C. 2018, PhRvL, 120, 205102
Klein, K. G., Howes, G. G., TenBarge, J. M., et al. 2012, ApJ, 755, 159
Klein, K. G., Howes, G. G., & Tenbarge, J. M. 2017, JPlPh, 83, 535830401
Lepping, R. P., Acũna, M. H., Burlaga, L. F., et al. 1995, SSRv, 71, 207
Li, X., & Habbal, S. R. 2000, JGR, 105, 7483
Marsch, E., & Livi, S. 1987, JGR, 92, 7263
Marsch, E., Rosenbauer, H., Schwenn, R., Muehlhaeuser, K. H., & Neubauer, F. M. 1982, JGR, 87, 35
Maruca, B. A. 2012, PhD thesis, Harvard University
Maruca, B. A., Bale, S. D., Sorriso-Valvo, L., Kasper, J. C., & Stevens, M. L. 2013, PhRvL, 111, 241101
Maruca, B. A., Kasper, J. C., & Bale, S. D. 2011, PhRvL, 107, 201101
Meyrand, R., Kanekar, A., Dorland, W., & Schekochihin, A. A. 2019, PNAS, 116, 1185
Mostafavi, P., Allen, R. C., McManus, M. D., et al. 2022, ApJL, 926, L38
Narita, Y., & Marsch, E. 2015, ApJ, 805, 24
Neugebauer, M., Goldstein, B. E., Smith, E. J., & Feldman, W. C. 1996, JGR, 101, 17047
Nicolaou, G., Livadiotis, G., Wicks, R. T., Verscharen, D., & Maruca, B. A. 2020, ApJ, 901, 26
Ofman, L., Boardsen, S. A., Jian, L. K., Verniero, J. L., & Larson, D. 2022, ApJ, 926, 185
Ofman, L., & Viñas, A. F. 2007, JGRA, 112, A06104
Ogilvie, K. W., Chornay, D. J., Fritzenreiter, R. J., et al. 1995, SSRv, 71, 55
Parker, J. T., Highcock, E. G., Schekochihin, A. A., & Dellar, P. J. 2016, PhPl, 23, 070703
Riquelme, M. A., Quataert, E., & Verscharen, D. 2015, ApJ, 800, 27
Robbins, D. E., Hundhausen, A. J., & Bame, S. J. 1970, JGR, 75, 1178
Šafrankova, J., Němecek, Z., Němec, F., et al. 2021, ApJ, 913, 80
Schekochihin, A. A., Cowley, S. C., Dorland, W., et al. 2009, ApJS, 182, 310
Schekochihin, A. A., Parker, J. T., Highcock, E. G., et al. 2016, JPlPh, 82, 905820212
Stansby, D., Perrone, D., Matteini, L., Horbury, T. S., & Salem, C. S. 2019, A&A, 623, L2
Tu, C. Y., & Marsch, E. 1995, SSRv, 73, 1
Verscharen, D., Bourouaine, S., Chandran, B. D. G., & Maruca, B. A. 2013a, ApJ, 773, 8
Verscharen, D., Bourouaine, S., & Chandran, B. D. G. 2013b, ApJ, 773, 163
Verscharen, D., Chandran, B. D. G., Bourouaine, S., & Hollweg, J. V. 2015, ApJ, 806, 157
Verscharen, D., Chandran, B. D. G., Klein, K. G., & Quataert, E. 2016, ApJ, 831, 128
Verscharen, D., Chen, C. H. K., & Wicks, R. T. 2017, ApJ, 840, 106
Xie, H.-s 2014, CoPhC, 185, 670
Yao, S., He, J. S., Marsch, E., et al. 2011, ApJ, 728, 146
Yao, S., He, J. S., Tu, C. Y., Wang, L. H., & Marsch, E. 2013, ApJ, 774, 59
Zhao, G. Q., Feng, H. Q., Wu, D. J., et al. 2018, JGRA, 123, 1715